nature photonics

SUPPLEMENTARY INFORMATION

DOI: 10.1038/NPHOTON.2013.31

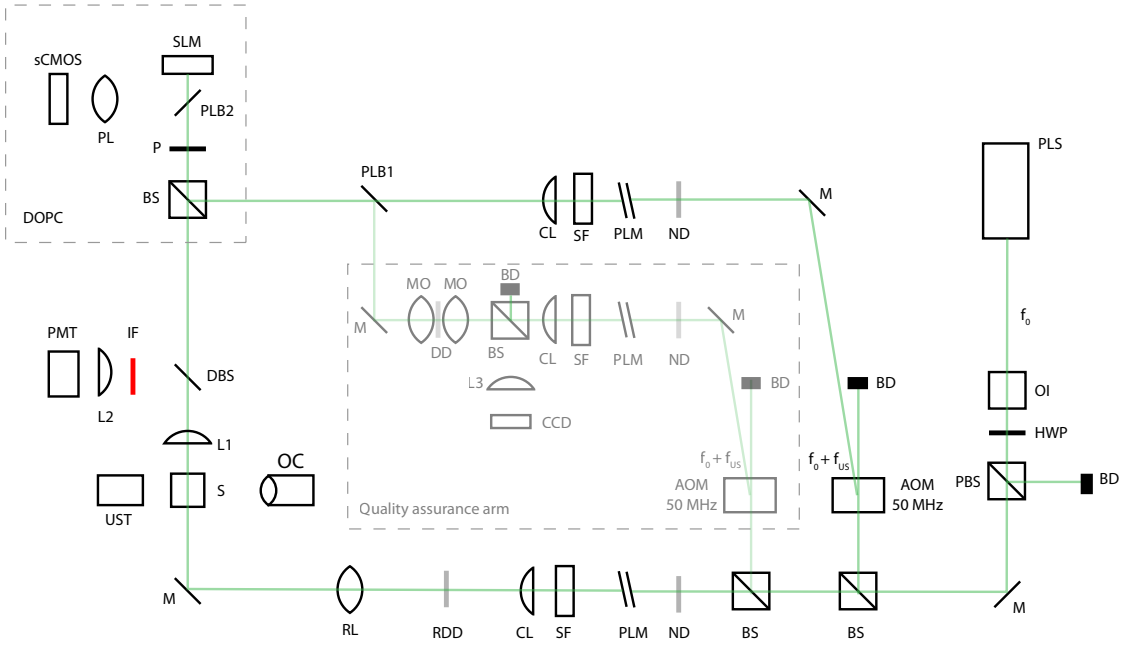

Supplementary Figure 1 | Setup diagram: Abbreviations: Pulsed laser source (PLS), Optical Isolator (OI), Half-wave plate (HWP), Polarizing beamsplitter (PBS), Beam dump (BD), Mirror (M), 50/50 cube beamsplitter (BS), Acousto-optic modulator (AOM), Neutral density filter-wheel (ND), Path length matching arm (PLM), Single-mode fiber acting as spatial filter (SF), Collimating lens (CL), Sample (S), Ultrasound transducer (UST), 50 mm planoconvex lens (L1), Dichroic beamsplitter (DBS), Interference filter (IF), 25 mm planoconvex lens (L2), Photomultiplier tube (PMT), Polarizer (P), 90/10 plate beamsplitter (PLB1), Digital optical phase conjugation setup (DOPC), 50/50 plate beamsplitter (PLB2), Photography compound lens (PL), sCMOS camera (sCMOS), Spatial light modulator (SLM), 300 mm plano-convex lens (L3), Microscope objective (MO), Diffuser disk (DD), Diffuser Disk on Rotation mount (RDD), Relay lens system (RL) imaging the illumated spot on the diffuser disk onto the sample (RL), Observing camera (OC)

DOI: 10.1038/NPHOTON.2013.31

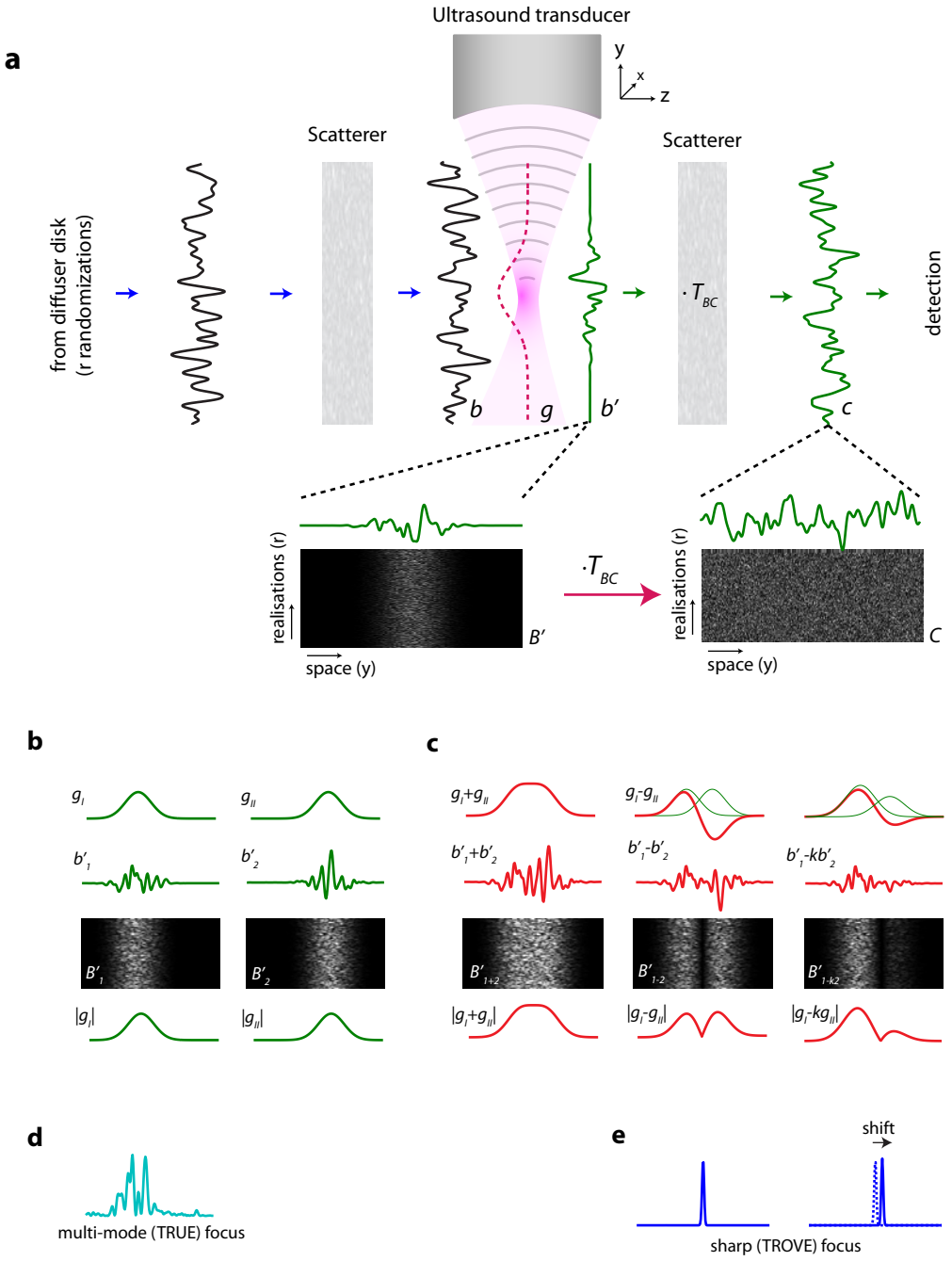

Supplementary Figure 2 | Variance encoding of optical transmission modes. a, Schematic of the scattering process and the setup: An input wavefront illuminates the sample and is randomized as it reaches the ultrasound focal plane (represented as a 1D vector *b*). A fraction of the randomized wavefront passing the Gaussian-shaped ultrasound focus (*g*) gets frequency-shifted by the acousto-optic effect (*b′*), before propagating through the second tissue section (represented by the scattering matrix T_{BC}). The frequency-shifted wavefront leaving the tissue (*c*) is then selectively detected using digital phase-shifting holography. As the input wavefront reaching the sample is randomized by rotating a diffuser disk, all realizations of the wavefronts can be inserted into the rows of one data matrix for each plane. **b,** Exemplary shifted ultrasound foci $g_{1,2}$, wavefronts $b'_{1,2}$ and data sets $B'_{1,2}$ (displaying the absolute of the complex valued matrices). Due to the complex normal statistics of speckle, the expected variance along the columns of $B'_{1,2}$ is $|g_{1,2}|^2$. **c,** Sum (left) and difference (middle and right) data sets calculated from the two data sets shown in panel b. Note that the expected variance along columns of B'_{1-2} and B'_{1+2} will follow $|g_1-g_2|^2$ and $|g_1+g_2|^2$, respectively. Right: difference of differenctially weighted datasets, with shifted null-point of variance **d,** Simulation of regular time reversal (TRUE focusing), resulting in a speckled optical focus the size of the ultrasound focus. **e,** Simulation of time reversal of variance-encoded light (TROVE), resulting in a focus the size of an individual speckle, which can be computationally shifted. (Plots show normalized intensity).

Supplementary Note

Simulations

As a first confirmation of our ability to encode and decode individual spatial transmission modes, we implemented the TROVE framework in a numerical simulation (see Supp. Fig. 2a). As shown in Supp. Fig. 2b, we generated complex random (normally distributed) matrices $\boldsymbol{B}$ and $\boldsymbol{T_{BC}}$ and chose two overlapping 1-D Gaussian functions $\boldsymbol{g_1}$ and $\boldsymbol{g_2}$, representing the shifted ultrasound foci that convert $\boldsymbol{B}$ into $\boldsymbol{B'_1}$ and $\boldsymbol{B'_2}$, respectively (see supplementary methods for details). We then calculated the matrices $\boldsymbol{C_1}$ and $\boldsymbol{C_2}$ that would have been measured outside the scattering medium in a real experiment. With the decoding strategy outlined in the Methods section, using only $\boldsymbol{C_1 - C_2}$, we calculated the vector $\boldsymbol{v}$ that maximized the ratio of variances along $\boldsymbol{C_{1+2}}$ and $\boldsymbol{C_{1-2}}$ (Supp. Fig. 1c). When this vector was time-reversed (multiplied by $\boldsymbol{T_{BC}}^*$ in the simulation), we were able to achieve a tight speckle-sized focus at the intersection of the two functions $\boldsymbol{g_1}$ and $\boldsymbol{g_2}$ (see Supp. Fig. 2e). Comparatively, when we simulated the TRUE framework by time-reversing one row of either the $\boldsymbol{C_1}$ or the $\boldsymbol{C_2}$ matrix, we found that the resultant field consisted of a multi-mode focus, the size of the much larger Gaussian-shaped ultrasound ($\boldsymbol{g_1}$ or $\boldsymbol{g_2}$) (Supp. Fig. 2d).

The simulations of TRUE and TROVE focusing described above were implemented using custom routines written in MATLAB (The Mathworks). The simulations were divided into three modules: First, we generated the complex random matrices $\boldsymbol{B_{1,2}}$ (1000 repetitions by 200 pixels at ultrasound plane) and $\boldsymbol{T_{BC}}$ (200 pixels at ultrasound plane by 1000 pixels at the detection plane; the size of $\boldsymbol{T_{BC}}$ was chosen to be as large as the memory of our computer would permit). To simulate speckle autocorrelation, we convolved $\boldsymbol{B_{1,2}}$ with a speckle autocorrelation function (a Gaussian of FWHM = 5). We then chose Gaussian functions representing $g_{1,2}$ the ultrasound foci (FWHM = 50, σ = 21, shifted by 2σ) and calculated the matrices $\boldsymbol{C_{1,2}} = \boldsymbol{B \cdot G_{1,2} \cdot T_{BC}}$. Second, we performed the same analysis on $\boldsymbol{C_{1,2}}$ which we also performed on experimentally measured data to obtain the vector $\boldsymbol{v}$ maximizing the Rayleigh quotient (see above). Third, we simulated time reversal of this vector by multiplying its complex conjugate by $\boldsymbol{T_{BC}}^T$. Finally, the time-reversed focus was moved by computationally shifting the intersection point between

DOI: 10.1038/NPHOTON.2013.31

the two Gaussian foci. This is achieved by changing the scalar k in the equation $\boldsymbol{C_{1\text{-}2} = C_1 - kC_2}$. The intersection between $\boldsymbol{g_1}$ and $k \cdot \boldsymbol{g_2}$ could be shifted predictably according to $k = 2e^{x/\sigma}$ (where $\boldsymbol{g_1}$ and $\boldsymbol{g_2}$ are Gaussian functions whose means are separated by 2σ, and x is the shift of the intersection point).

Derivation of a computationally efficient decoding algorithm

The proposed eigenvalue formula used to determine the optimal phase pattern $\boldsymbol{v}^*$ to display on the spatial light modulator, given an acquired data set, is justified as follows. We limit this proof to a two dimensional geometry, with straightforward extension to three dimensions. We assume the scattering events between the ultrasound focus at the ultrasound plane and the detector at the output plane are represented by a transmission matrix $\boldsymbol{T}$. The detector collects m measurements across n pixels of speckle data with the ultrasound focus located first at position 1, and then at position 2. We assume the underlying speckle field along $\boldsymbol{b}$ does not change between measurements with the ultrasound focus at these two different locations. This allows us to express the recorded data with a shared underlying speckle data matrix, $\boldsymbol{B}$, modified by two different Gaussian envelopes representing the ultrasound at two different positions, described by diagonal matrices $\boldsymbol{G_1}$ and $\boldsymbol{G_2}$, respectively. The two calculated data matrices of interest are,

$$\boldsymbol{C_{1+2} = BG_1T + BG_2T = BG_{1+2}T} \quad (1)$$

$$\boldsymbol{C_{1\text{-}2} = BG_1T - BG_2T = BG_{1\text{-}2}T}, \quad (2)$$

where $\boldsymbol{G_1}$ and $\boldsymbol{G_2}$ are n x n square with a shifted Gaussian function along the diagonal and zeros elsewhere. $\boldsymbol{G_{1+2}}$ and $\boldsymbol{G_{1\text{-}2}}$ are also square diagonal matrices containing the Gaussian functions' sum and difference, respectively. The m x n underlying data matrix $\boldsymbol{B}$ contains independent speckle field measurements along its rows. Note that due to our ordering of matrices, the spatial covariance matrix of the above data will take the form $\boldsymbol{CC}^*$, while the data's Gram matrix will take the form $\boldsymbol{C}^*\boldsymbol{C}$, which is opposite from common notation.

As discussed in the main text, TROVE's computational goal is to identify a single mode at the ultrasound plane corresponding to the intersection of the two Gaussian ultrasound envelopes centred at g_1 and g_2.

This goal is achieved by finding a vector $\boldsymbol{v}$ along which the variance of $\boldsymbol{C}_{1+2}$ is maximal and the variance of $\boldsymbol{C}_{1-2}$ is minimal. Such a vector $\boldsymbol{v}$ will maximize the Rayleigh Quotient Q of the covariance matrices of the two datasets, $\boldsymbol{C}_{1-2}{}^{*}\boldsymbol{C}_{1-2}$ and $\boldsymbol{C}_{1+2}{}^{*}\boldsymbol{C}_{1+2}$:

$$Q = \boldsymbol{v}^{*}\boldsymbol{C}_{1+2}{}^{*}\boldsymbol{C}_{1+2}\boldsymbol{v}/(\boldsymbol{v}^{*}\boldsymbol{C}_{1-2}{}^{*}\boldsymbol{C}_{1-2}\,\boldsymbol{v}). \quad (3)$$

The maximization of the Rayleigh Quotient above is associated with a solution to the generalized eigensystem,

$$\boldsymbol{C}_{1+2}{}^{*}\boldsymbol{C}_{1+2}\boldsymbol{v} = \boldsymbol{C}_{1-2}{}^{*}\boldsymbol{C}_{1-2}\lambda\boldsymbol{v}, \quad (4)$$

with eigenvalue λ. We express the eigenvector $\mathbf{v}$ associated with the maximum eigenvalue λ of this general eigensystem as,

$$\boldsymbol{v} = \mathrm{eig}[(\boldsymbol{C}_{1-2}{}^{*}\boldsymbol{C}_{1-2})^{-1}\boldsymbol{C}_{1+2}{}^{*}\boldsymbol{C}_{1+2}], \quad (5)$$

where eig[] represents a principal eigenvector identification operator. In practice, due to the high n x n dimensionality of the spatial covariance matrices $\boldsymbol{C}_{1+2}{}^{*}\boldsymbol{C}_{1+2}$ and $\boldsymbol{C}_{1-2}{}^{*}\boldsymbol{C}_{1-2}$, Eq. (5) is difficult to computationally evaluate. Instead, we desire an eigenvector solution based on the much smaller m x m Gram matrices $\boldsymbol{C}_{1+2}\boldsymbol{C}_{1+2}{}^{*}$ and $\boldsymbol{C}_{1-2}\boldsymbol{C}_{1-2}{}^{*}$.

We apply two approximations about the structure of the recorded speckle data to determine a computational solution based on two m x m Gram matrices. First, we suppose that the complex random Gaussian transmission matrix $\boldsymbol{T}$ satisfies $\boldsymbol{T}\boldsymbol{T}^{*} \approx \boldsymbol{I}$. This approximation commonly underlies phase conjugation experiments, and the associated error approaches zero as $\boldsymbol{T}$ increases in size (i.e. more transmitted speckles are measured and phase conjugated) – as long as long-range (C_2) and infinite-range (C_3) correlations can be neglected (Phys. Rev. Lett. 64, 2787-2790 (1990)). Such higher-order correlations may be neglected in samples with many open channels, including those used in our experiments as well as biological tissue. Second, we also assume the matrix $\boldsymbol{B}$ comprising the many recorded underlying speckle fields at the ultrasound focus is also complex random Gaussian. As the recorded data matrix is rectangular (m x n, $n > m$), this leads us to the approximations $\boldsymbol{B}^{*}\boldsymbol{B} \approx \boldsymbol{I}_{nxn}$ and $\boldsymbol{B}\boldsymbol{B}^{*}$

DOI: 10.1038/NPHOTON.2013.31

$\approx \boldsymbol{I}_{mxm}$, where $\boldsymbol{I}$ is the identity matrix, following the same approximation applied to T. The latter approximation improves as m approaches n.

Proceeding with the derivation, we first move $\boldsymbol{C}_{1\text{-}2}^{*}\boldsymbol{C}_{1\text{-}2}$ in Eq. (4) to the left side by taking its inverse:

$$(\boldsymbol{C}_{1\text{-}2}^{*}\boldsymbol{C}_{1\text{-}2})^{-1}\boldsymbol{C}_{1+2}^{*}\boldsymbol{C}_{1+2}\boldsymbol{v} = \lambda\boldsymbol{v}. \tag{6}$$

Then, plugging Eq. (1) and Eq. (2) into Eq. (6) leads to,

$$(\boldsymbol{T}^{*}\boldsymbol{G}_{1\text{-}2}\boldsymbol{B}^{*}\boldsymbol{B}\boldsymbol{G}_{1\text{-}2}\boldsymbol{T})^{-1}(\boldsymbol{T}^{*}\boldsymbol{G}_{1+2}\boldsymbol{B}^{*}\boldsymbol{B}\boldsymbol{G}_{1+2}\boldsymbol{T})\boldsymbol{v} = \lambda\boldsymbol{v}. \tag{7}$$

Applying our second approximation that $\boldsymbol{B}^{*}\boldsymbol{B} = \boldsymbol{I}$, this simplifies to,

$$(\boldsymbol{T}^{*}\boldsymbol{G}_{1\text{-}2}^{2}\boldsymbol{T})^{-1}(\boldsymbol{T}^{*}\boldsymbol{G}_{1+2}^{2}\boldsymbol{T})\,\boldsymbol{v} = \lambda\boldsymbol{v}. \tag{8}$$

Evaluating the inverse and using our first approximation that $\boldsymbol{T}^{-1} = \boldsymbol{T}^{*}$ leads to,

$$\boldsymbol{T}^{*}\boldsymbol{G}_{1\text{-}2}^{-2}\boldsymbol{G}_{1+2}^{2}\boldsymbol{T}\boldsymbol{v} = \lambda\boldsymbol{v}. \tag{9}$$

Here, $\boldsymbol{G}_{1\text{-}2}^{-2}$ is a square matrix with $\boldsymbol{G}_{1\text{-}2}^{-2}(i,j) = 1/\boldsymbol{G}_{1\text{-}2}^{2}(i,j)$ for all $i=j$ and $\boldsymbol{G}_{1\text{-}2}^{-2}(i,j) = 0$ for all $i\sim=j$. Eq. (9) can be transformed from an n x n matrix eigensystem to a smaller m x m matrix eigensystem by attempting to solve for a new eigenvector $\boldsymbol{y}$, where $\boldsymbol{v} = \boldsymbol{T}^{*}\boldsymbol{B}^{*}\boldsymbol{y}$. Plugging this relationship into Eq. (9) yields,

$$\boldsymbol{T}^{*}\boldsymbol{G}_{1\text{-}2}^{-2}\boldsymbol{G}_{1+2}^{2}\,\boldsymbol{T}(\boldsymbol{T}^{*}\boldsymbol{B}^{*}\boldsymbol{y}) = \lambda(\boldsymbol{T}^{*}\boldsymbol{B}^{*}\boldsymbol{y}). \tag{10}$$

Applying our first approximation to the left side and then multiplying both sides by $\boldsymbol{T}$ from the left leads to,

$$\boldsymbol{G}_{1\text{-}2}^{-2}\,\boldsymbol{G}_{1+2}^{2}\boldsymbol{B}^{*}\boldsymbol{y} = \boldsymbol{B}^{*}\lambda\boldsymbol{y}. \tag{11}$$

Multiplying by an additional factor $\boldsymbol{B}$ from the left on either side and applying our second approximation to the right side leads to,

$$\boldsymbol{B}\boldsymbol{G}_{1\text{-}2}^{-2}\boldsymbol{G}_{1+2}^{2}\boldsymbol{B}^{*}\boldsymbol{y} = \lambda\boldsymbol{y}. \tag{12}$$

Again, following our approximation that $\boldsymbol{B}^{*}\boldsymbol{B} = \boldsymbol{I}$, we can insert this term into the middle of Eq. (12) to produce,

$$(\boldsymbol{B}\boldsymbol{G}_{1\text{-}2}{}^{-2}\boldsymbol{B}^{*})(\boldsymbol{B}\,\boldsymbol{G}_{1+2}{}^{2}\boldsymbol{B}^{*})\boldsymbol{y} = \lambda\boldsymbol{y}. \tag{13}$$

$\boldsymbol{G}_{1\text{-}2}{}^{-2}$ is a diagonal matrix, and under our second assumption $\boldsymbol{B}$ and $\boldsymbol{B}^{*}$ setup an orthogonal basis for the term in parentheses on the left. Thus, Eq. (13) is equivalent to,

$$(\boldsymbol{B}\boldsymbol{G}_{1\text{-}2}{}^{2}\boldsymbol{B}^{*})^{-1}\,(\boldsymbol{B}\boldsymbol{G}_{1+2}{}^{2}\boldsymbol{B}^{*})\boldsymbol{y} = \lambda\boldsymbol{y}. \tag{14}$$

Here, we see that the two terms in the parenthesis can be expressed in terms of the original data matrices $\boldsymbol{C}_{1+2}$ and $\boldsymbol{C}_{1\text{-}2}$ as,

$$(\boldsymbol{C}_{1\text{-}2}\boldsymbol{C}_{1\text{-}2}{}^{*})^{-1}(\boldsymbol{C}_{1+2}\boldsymbol{C}_{1+2}{}^{*})\boldsymbol{y} = \lambda\boldsymbol{y}, \tag{15}$$

which is the desired re-expression of the eigensystem in Eq. (4) in terms of the smaller m x m Gram matrices $\boldsymbol{C}_{1+2}\boldsymbol{C}_{1+2}{}^{*}$ and $\boldsymbol{C}_{1\text{-}2}\boldsymbol{C}_{1\text{-}2}{}^{*}$. Our first approximation is used once more while transforming Eq. (14) to Eq. (15). We can find the originally desired eigenvector $\boldsymbol{v}$ associated with the largest eigenvalue λ by solving Eq. (15) for the largest eigenvector $\boldsymbol{y}$, and then solving $\boldsymbol{v} = \boldsymbol{T}^{*}\boldsymbol{B}^{*}\boldsymbol{y}$:

$$\boldsymbol{v} = \boldsymbol{T}^{*}\boldsymbol{B}^{*}\cdot\mathrm{eig}[(\boldsymbol{C}_{1\text{-}2}\boldsymbol{C}_{1\text{-}2}{}^{*})^{-1}(\boldsymbol{C}_{1+2}\boldsymbol{C}_{1+2}{}^{*})\,] = (\boldsymbol{B}\boldsymbol{T})^{*}\cdot\mathrm{eig}[(\boldsymbol{C}_{1\text{-}2}\boldsymbol{C}_{1\text{-}2}{}^{*})^{-1}(\boldsymbol{C}_{1+2}\boldsymbol{C}_{1+2}{}^{*})]. \tag{16}$$

Since the experiment does not allow direct access to the data matrix $\boldsymbol{B}\boldsymbol{T}$, we use the approximation $\boldsymbol{B}\boldsymbol{G}_{1+2}\boldsymbol{T} \approx \boldsymbol{B}\boldsymbol{T}$ to instead generate the approximate eigenvector evaluation,

$$\boldsymbol{v} \approx \boldsymbol{C}_{1+2}{}^{*}\cdot\mathrm{eig}[(\boldsymbol{C}_{1\text{-}2}\boldsymbol{C}_{1\text{-}2}{}^{*})^{-1}(\boldsymbol{C}_{1+2}\boldsymbol{C}_{1+2}{}^{*})] \tag{17}$$

This final approximation is justified as follows. We should expect a successful solution to Eq. (16) to take the general form $\boldsymbol{v} = (\boldsymbol{d}(x)\cdot\boldsymbol{T})^{*}$, where $\boldsymbol{d}(x)$ is a row vector with 1 in row x and 0's elsewhere. This is supported by the intuitive notion that our goal is to refocus to a small delta function-like spot at a position x, which is equivalent to determining one row of $\boldsymbol{T}$. Under such an assumption, inserting a diagonal matrix $\boldsymbol{G}$ between $\boldsymbol{d}(x)$ and $\boldsymbol{T}$ does not alter their matrix product up to a constant scaling factor, given $\boldsymbol{G}(x,x)$ is non-zero, which is guaranteed by setting $\boldsymbol{G}=\boldsymbol{G}_{1+2}$ and ensuring the desired mode x is near the intersection of the two summed Gaussians.

Finally, for computational efficiency, the above equation can be rewritten to involve an eigendecomposition of a Hermitian matrix:

DOI: 10.1038/NPHOTON.2013.31

$$\boldsymbol{v} \approx \boldsymbol{C}_{1+2}^{*} \cdot (\boldsymbol{C}_{1\text{-}2}\boldsymbol{C}_{1\text{-}2}^{*})^{-1/2} \cdot \mathrm{eig}[(\boldsymbol{C}_{1\text{-}2}\boldsymbol{C}_{1\text{-}2}^{*})^{-1/2}(\boldsymbol{C}_{1+2}\boldsymbol{C}_{1+2}^{*})(\boldsymbol{C}_{1\text{-}2}\boldsymbol{C}_{1\text{-}2}^{*})^{-1/2}] \quad (18)$$

No additional approximations are required to obtain Eq. (18) from Eq. (17).

This derivation can be easily extended to the 2D case, where we find $\boldsymbol{v}$ along which the variance of $\boldsymbol{C}_{1+2+3+4}$ is maximal and the sum of the variances of $\boldsymbol{C}_{1\text{-}4}$ and $\boldsymbol{C}_{2\text{-}3}$ is minimal, obtaining:

$$\boldsymbol{v} \approx \boldsymbol{C}_{1+2+3+4}^{*} \cdot (\boldsymbol{C}_{1\text{-}4}\boldsymbol{C}_{1\text{-}4}^{*} + \boldsymbol{C}_{2\text{-}3}\boldsymbol{C}_{2\text{-}3}^{*})^{-1/2} \cdot \mathrm{eig}[(\boldsymbol{C}_{1\text{-}4}\boldsymbol{C}_{1\text{-}4}^{*} + \boldsymbol{C}_{2\text{-}3}\boldsymbol{C}_{2\text{-}3}^{*})^{-1/2}(\boldsymbol{C}_{1+2+3+4}\boldsymbol{C}_{1+2+3+4}^{*})(\boldsymbol{C}_{1\text{-}4}\boldsymbol{C}_{1\text{-}4}^{*} + \boldsymbol{C}_{2\text{-}3}\boldsymbol{C}_{2\text{-}3}^{*})^{-1/2}] \quad (19)$$

Preservation of variance

The main article refers to the fact that variance across realizations is preserved as modes propagate through a scatter. We derive and justify the statement as follows: We note that the covariance of realizations in the dataset $\boldsymbol{B'}$ is expressed as $\boldsymbol{B'B'}^{*}$. Using the approximation $\boldsymbol{TT}^{*} \approx \boldsymbol{I}$ described above, we can derive

$$\boldsymbol{CC}^{*} = (\boldsymbol{B'T})(\boldsymbol{B'T})^{*} = \boldsymbol{B'TT}^{*}\boldsymbol{B'}^{*} \approx \boldsymbol{B'B'}^{*} \quad (20)$$

This equation states that the realizations covariance at the ultrasound plane can be approximated by the realizations covariance at the output plane.

Scanning / orthogonalisation of modes

To ensure separation between spatial modes corresponding to nearby points in the ultrasound plane, we used the following orthogonalisation strategy: First, by weighing the data matrices as described above, we obtained 100 optical modes $\boldsymbol{v}$, corresponding to a 2D 6 x 6 grid of points at the XY-plane at the ultrasound focus (grid spacing: 5μm) and created a matrix $\boldsymbol{V}$ containing all vectors $\boldsymbol{v}$ in its columns. We then orthogonalised this matrix with the aid of its singular value decomposition: $\boldsymbol{V} = \boldsymbol{PQR'}$, where $\boldsymbol{Q}$ is a diagonal matrix, and $\boldsymbol{P}$ and $\boldsymbol{R}$ are orthogonal matrices. The orthogonalised version of $\boldsymbol{V}$ was then calculated as $\boldsymbol{V_o} = \boldsymbol{PR}'$. When each of the columns of $\boldsymbol{V}_o$ was time-reversed, we achieved focusing to the corresponding point on a grid with 5μm separation. To obtain a final 12 x 12 grid with 2.5 μm spacing, we performed the above procedure 4 times with shifted grids (with (0/2.5) μm shift in X and (0/2.5) μm shift in Y).